

Local structure memory effects in the polar and nonpolar phases of MoTe₂

Valeri Petkov^{1,*} and Yang Ren²

¹*Department of Physics, Central Michigan University, Mt. Pleasant, Michigan 48858, USA*

²*X-ray Science Division, Advanced Photon Source, Argonne National Laboratory, Argonne, Illinois 60439, USA*

 (Received 7 January 2021; revised 12 February 2021; accepted 15 February 2021; published 1 March 2021)

We use total scattering to study the reversible transition between the polar $1T'$ and nonpolar T_d phases of layered MoTe₂ taking place at 240 K. Whereas, macroscopically, the transition appears to be first order, locally, it is not. In particular, a great deal of the stacking sequence of Te-Mo-Te layers characteristic of the polar $1T'$ phase persists locally in the nonpolar T_d phase, and vice versa, over a broad temperature range extending about 100 K both below and above the transition. The intermixing ratio for the two sequences evolves gradually across the transition temperature, consistent with a second-order transition behavior. The presence of coexisting local polar and nonpolar regions and the resulting variety of internal interfaces where the spatial inversion symmetry is broken may be behind some of the unusual electronic properties of T_d -MoTe₂, including its putative type-II Weyl semimetal state.

DOI: [10.1103/PhysRevB.103.094101](https://doi.org/10.1103/PhysRevB.103.094101)

I. INTRODUCTION

Transition-metal chalcogenides (TMDs) have attracted an immense interest due to their fascinating properties and promise for practical applications. A typical example is MoTe₂, which has been reported to exhibit giant magnetoresistance [1–4], nonlinear Hall effect [5–10], tunable polar domains [11–13], and superconductivity that is strongly influenced both by pressure and doping [11,14,15]. The material has also been suggested to exhibit properties of a type-II Weyl semimetal, an exotic quantum state of matter, where the so-called Weyl points appear at the intersections between hole and electron pockets [16–23]. It is generally believed that the unique properties of MoTe₂ are rooted in its specific layered structure, rich phase diagram, and structural tunability [24–27].

In particular, at room temperature, MoTe₂ crystallizes in a centrosymmetric hexagonal ($2H$) space group (S.G.) $P6_3/mmc$ -type structure, where a perfect trigonal prism of Te atoms surrounds each Mo atom. At high temperature (>1175 K), it adopts a centrosymmetric monoclinic ($1T'$) S.G. $P2_1/m$ type structure, where each Mo atom is surrounded by an octahedron of Te atoms, but is shifted away from its center. The shift is due to metal-metal interactions and results in the formation of zigzag chains of Mo atoms [28–30]. Notably, MoTe₂ is unique among the TMDs because it can be grown in both the stable $2H$ and unstable $1T'$ polymorphs at room temperature. When cooled down to about 240 K, the latter undergoes a phase transition into a noncentrosymmetric orthorhombic (T_d) S.G. $Pnm2_1$ type structure [31]. In all three polymorphs, Mo and Te atoms form triple Te-Mo-Te layers, which stack along the c axis of the unit cell and interact via weak van der Waals forces. The layers are perfect in $2H$ -MoTe₂ and corrugated in $1T'$ -MoTe₂

due to the metal-metal interaction. The interactions distort Mo-Te₆ octahedra in the latter, causing the c axis to incline at a monoclinic angle β of about 93.8° to the layers. As illustrated in Figs. 1(a) and 1(b), orthorhombic T_d -MoTe₂ is built from the same layers of distorted Mo-Te₆ octahedra as $1T'$ -MoTe₂ is but exhibits a vertical layer stacking sequence ($\beta = 90^\circ$). Due to their distinctly different atomic structure, $2H$ -MoTe₂ appears semiconducting whereas $1T'$ -MoTe₂ and T_d -MoTe₂ appear semimetallic [32–34]. However, regardless the atomic structure of $1T'$ and T_d phases of MoTe₂ is similar, Weyl points may exist only in the latter because of the broken crystal inversion symmetry [17,18,35]. Accordingly, most recent studies have concentrated on T_d -MoTe₂. It has been observed that $1T'$ and T_d phases coexist over a wide temperature range extending on both sides of the transition temperature, suggesting that the energy barrier between them is small but significant and the crystal lattice is likely to be imperfect in that range [11,13,36]. The imperfections are indeed manifested by the presence of significant diffuse scattering in x-ray [31] and neutron-scattering data [37] obtained near the phase transition. Single-crystal studies showed that, at a macroscopic level, imperfections in TMDs, including MoTe₂, could involve crystal twinning and domain fragmentation [38]. On an atomic level, the imperfections could include unusual distortions of TM-chalcogenide polyhedral units and buckling of chalcogenide-TM-chalcogenide layers [39]. It has been recognized that, due to the weak interlayer interaction, the imperfections in TMDs are also likely to include stacking faults, involving sliding and rotation of individual chalcogenide-TM-chalcogenide layers [40]. The nature of structural imperfections accompanying the $1T'$ - T_d phase transition in MoTe₂, however, is not well revealed because they have been largely studied by crystallographic techniques that are able to capture well the average crystal symmetry but may be less successful in revealing fine imperfections of the underlying crystal lattice. Knowledge of the imperfections and their temperature evolution is important for

*petko1vg@cmich.edu

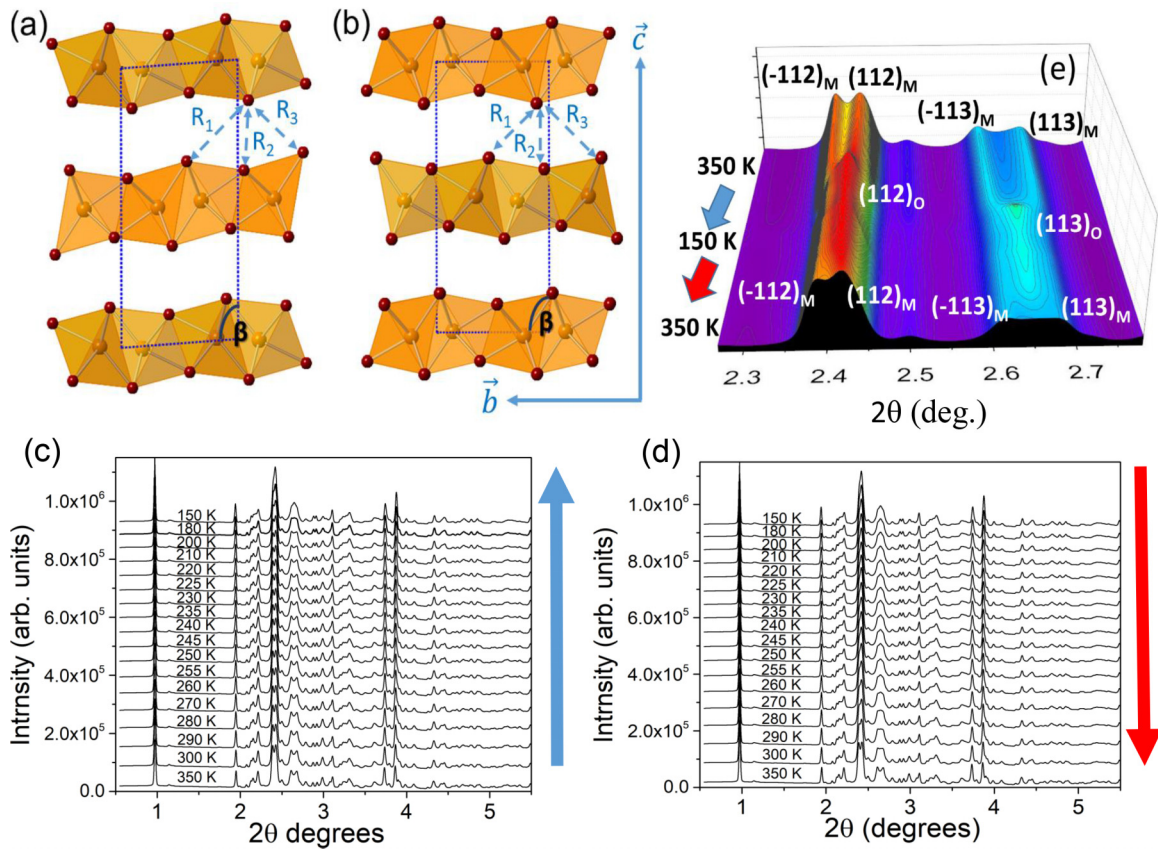


FIG. 1. Atomic structure of (a) monoclinic $1T'$ ($\beta = 93.8^\circ$) and (b) orthorhombic T_d ($\beta = 90^\circ$) phases of MoTe_2 projected on the (\vec{b}, \vec{c}) atomic plane. The respective unit cells are outlined with a broken blue line. The phases are built of corrugated layers of Mo-Te octahedra stacked along the \vec{c} axis of the unit cell, where the c -axis parameter of the unit cell for both phases is close to 14 Å. The layers are identical but positioned somewhat differently on top of each other in the different phases. Thus $R_1 (\sim 4.5 \text{ \AA}) > R_3 (\sim 3.9 \text{ \AA})$ and $R_3 (\sim 4.6 \text{ \AA}) > R_1 (\sim 3.9 \text{ \AA})$ for the $1T'$ and T_d phases, respectively (follow the blue arrows). In both phases, R_2 appears close to 3.80 Å. Mo atoms are in light brown and Te atoms are in red. The \vec{a} axis of the unit cell is perpendicular to the (\vec{b}, \vec{c}) atomic plane. Also, note that for clarity, the unit-cell orientation of the T_d structure is changed from the standard, $(\vec{a}, \vec{b}, \vec{c})$ S.G. $Pnm2_1$ setting to the symmetry equivalent $(\vec{b}, \vec{a}, \vec{c})$ S.G. $Pnm2_1$ setting. High-energy XRD patterns for MoTe_2 obtained (c) during cooling the sample down from 350 to 150 K (blue arrow) and then (d) warming it back to 350 K (red arrow). (e) Evolution of XRD features at Bragg angles of 2.4° and 2.65° with temperature. The feature at 2.4° in the XRD pattern of as-synthesized $1T'$ – MoTe_2 is split into two components at 350 K. The components can be indexed as $(-112)_M$ and $(112)_M$ Bragg peaks using a monoclinic (S.G. $P2_1/m$) lattice. The components merge into a single peak upon cooling down to 150 K, which can be indexed as $(112)_O$ Bragg peak using an orthorhombic (S.G. $Pnm2_1$) lattice. Furthermore, the feature at 2.65° in the XRD pattern of as-synthesized $1T'$ - MoTe_2 is split into two components at 350 K, which can be indexed as $(-113)_M$ and $(113)_M$ Bragg peaks using a monoclinic (S.G. $P2_1/m$) lattice. The components merge into a single peak upon cooling down to 150 K, which can be indexed as $(113)_O$ Bragg peak using an orthorhombic (S.G. $Pnm2_1$) lattice. Both $(112)_O$ and $(113)_O$ Bragg peaks split again upon a subsequent heating to 350 K, indicating that the recovered $1T'$ - MoTe_2 restores its monoclinic structure. The splitting, however, is less pronounced in comparison to that observed with as-synthesized $1T'$ - MoTe_2 .

clarifying the structural origin of the thermal hysteresis in the low-temperature properties of MoTe_2 and puzzling variations in the experimental data and theoretical predictions for the unusual electronic properties of T_d - MoTe_2 [21,22,41,42].

Here we use advanced x-ray scattering techniques that are applicable to systems with any type of lattice imperfections [43,44], including TMDs [39,45,46], to study the transition between the $1T'$ and T_d phases of MoTe_2 over a broad temperature range. We show that as-synthesized monoclinic $1T'$ - MoTe_2 does not exhibit significant structural imperfections at room temperature. Upon cooling to $T_c = 240 \text{ K}$, it undergoes a transition into a phase with an average orthorhombic crystal symmetry that, macroscopically, appears to be the T_d phase. The phase, however, exhibits

significant local structural imperfections arising from the presence of $1T'$ -type layer stacking sequence down to 150 K. In turn, upon warming, the layer stacking sequence characteristic of the orthorhombic T_d phase is preserved well above T_c , rendering the reconstructed $1T'$ phase locally imperfect in comparison to the pristine one. We argue that the observed phenomenon is a manifestation of a local atomic structure memory effect, where local structure features characteristic of the $1T'$ phase remain frozen in the T_d phase at least 100 K below T_c and such of the latter survive in the former up to about 100 K above T_c . The effect is likely to impact collective electronic states and related properties of T_d - MoTe_2 significantly and therefore ought to be accounted for in their considerations. The results expand

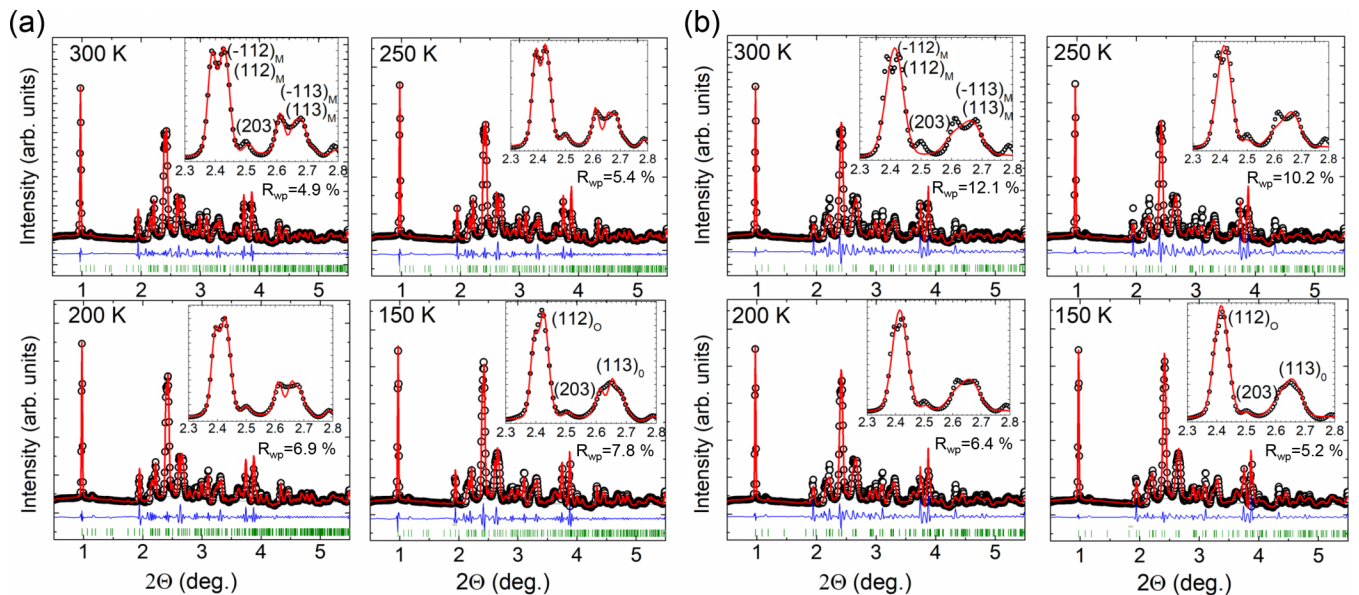


FIG. 2. Rietveld fits (red line) to high-energy XRD patterns (symbols) for MoTe_2 phases collected at different temperature during cooling the sample from 350 K down to 150 K. The residual difference (blue line) is shifted by adding a negative constant for clarity. Vertical green lines denote Bragg peaks in the respective model structures. Goodness of fit indicators, R_{wp} , are given for each dataset. Fits in (a) are based on the monoclinic (S.G. $P2_1/m$) structure exhibited by $1T'$ - MoTe_2 . Fits in (b) are based on the orthorhombic (S.G. $Pnm2_1$) structure exhibited by T_d - MoTe_2 . Diffraction features appearing in the angular range from 2.3° to 2.8° are shown in the inset. Miller indices assigned to the peaks are those defined in Fig. 1(c). Results in (a) show that the diffraction patterns collected at 300 and 250 K are well fit by the monoclinic $1T'$ structure. Refined monoclinic lattice parameters and atomic positions for these two fits are given as Supplemental Material [52]. The monoclinic structure model is less successful in describing the diffraction pattern collected at 200 K and particularly that collected at 150 K. Results in (b) show that the latter is fit relatively well by the T_d model. The model is less successful in describing the diffraction data collected at 200 K but still fits them to an acceptable level. The orthorhombic structure model, however, fails to fit the datasets collected above T_c ($= 240$ K). Refined orthorhombic lattice parameters and atomic positions for the fits to XRD data obtained below T_c are given as Supplemental Material [52]. Note that the Bragg peak profiles are not perfectly reproduced even by the successful fits to the datasets obtained at 150 K (T_d model) and 250 K ($1T'$ model). This is largely due to the presence of local structural imperfections such as stacking faults, which tend to distort the Bragg peak profiles [55,56] and are difficult to be accounted for in Rietveld analysis.

our knowledge about phase transitions in TMDs involving emergent quantum states of matter and also demonstrate an experimental approach to study them in fine structural detail.

II. EXPERIMENT

A high-quality $1T'$ - MoTe_2 sample was provided by 2DSemiconductors [47]. It was subjected to x-ray-diffraction (XRD) experiments using synchrotron x rays with energy of 105.7 keV ($\lambda = 0.1173 \text{ \AA}$). Scattered intensities were recorded using a 2D amorphous Si detector in a Debye-Scherrer geometry. The detector was positioned 1000 mm away from the sample to achieve high- q resolution, where the wave vector q is defined as $q = 4\pi \sin(\theta)/\lambda$ and θ is the Bragg angle. Here it may be added that, due to the azimuthal integration of the Debye-Scherrer rings, the use of a 2D detector helps not only to optimize the data collection time and improve the statistical accuracy of the XRD data but also minimize effects of preferred orientation on the data [46,48], which may occur in diffraction studies on layered materials such as MoTe_2 [49]. Data in a broad temperature range from 150 to 350 K were collected using Oxford Cryostream 700+ device to control the temperature of the sample. Diffraction patterns obtained during cooling the sample from 350 to 150

K and then warming it back to 350 K are summarized in Figs. 1(c) and 1(d), respectively. Bragg peaks in the diffraction patterns are sharp, reflecting their good resolution. Inspection of the patterns shows that several Bragg peaks change systematically with temperature. In particular, in as-synthesized MoTe_2 , the diffraction feature at 2.4° appears as a doublet, whose components can be indexed as $(-112)_M$ and $(112)_M$ peaks using a monoclinic (S.G. $P2_1/m$) lattice. The diffraction feature at 2.65° also appears as a doublet, whose components can be indexed as $(-113)_M$ and $(113)_M$ peaks using the same lattice, confirming the $1T'$ -type structure of the as-synthesized sample. The components merge into singlets with decreasing temperature, becoming, respectively, $(112)_O$ and $(113)_O$ Bragg peaks characteristic of an orthorhombic (S.G. $Pnm2_1$) lattice. The observation confirms that MoTe_2 acquires a T_d -type structure below 240 K. In line with the findings of other studies [11,31,50], the singlets split into doublets upon subsequent warming of the sample to room temperature, indicating that the reconstructed MoTe_2 phase restores its initial $1T'$ -type structure. The degree of splitting of the doublets in the XRD pattern of the reconstructed $1T'$ - MoTe_2 phase is less well expressed in comparison to as-synthesized $1T'$ - MoTe_2 phase [see Fig. 1(e)], indicating that the former is less perfect at atomic level in comparison to the latter.

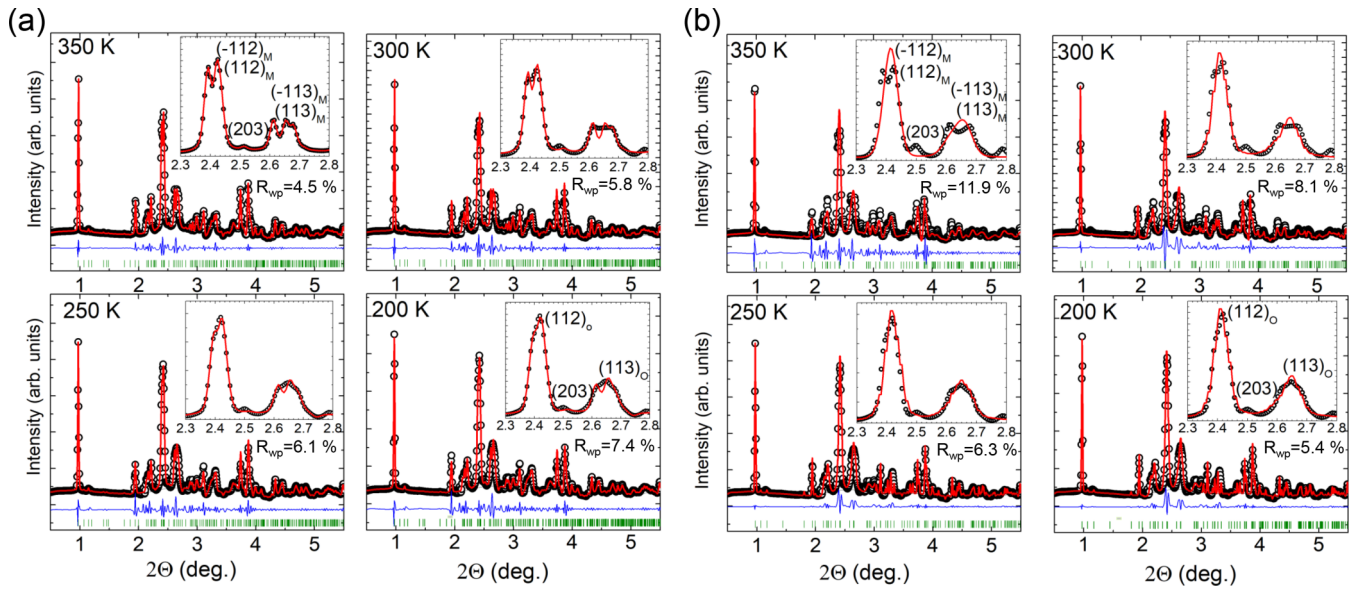


FIG. 3. Rietveld fits (red line) to high-energy XRD patterns (symbols) for MoTe₂ phases collected at different temperature during warming the sample from 150 to 350 K. The residual difference (blue line) is shifted by adding a negative constant for clarity. Vertical green lines denote Bragg peaks in the respective model structures. Goodness of fit indicators, R_{wp} , are given for each dataset. Fits in (a) are based on the monoclinic (S.G. $P2_1/m$) structure exhibited by $1T'$ -MoTe₂. Fits in (b) are based on the orthorhombic structure (S.G. $Pnm2_1$) exhibited by T_d -MoTe₂. Bragg peaks appearing in the angular range from 2.3° to 2.8° are shown in the inset. Miller indices assigned to the peaks are those defined in Fig. 1(e). Results in the plots show that the diffraction pattern collected at 200 K is quite well fit by the orthorhombic T_d model. The diffraction pattern obtained at 250 K is somewhat better fit by the $1T'$ structure model in comparison to the T_d model. Refined lattice parameters and atomic positions for these two fits are given as Supplemental Material [52]. The $1T'$ model clearly outperforms the T_d one in the case of data collected at 300 K upon warming. The quality of fit, however, is inferior in comparison to the pattern for as-synthesized sample also collected at 300 K but upon cooling [compare with data in Fig. 2(a)]. The diffraction pattern collected at 350 K is very well reproduced by the monoclinic $1T'$ -type model. The same is true for the respective PDF data set shown in Supplemental Fig. S2 [52]. Refined monoclinic lattice parameters and atomic positions for the $1T'$ model fits to XRD patterns collected at 300 K and 350 K are also given as Supplemental Material [52]. Note that the Bragg peak profiles are not perfectly reproduced even by the successful fits to the datasets obtained at 300 K ($1T'$ model), 250 K (both models), and 200 K (T_d model). This is due to the presence of structural imperfections such as stacking faults, which tend to distort the Bragg peak profiles [55,56] and are difficult to be accounted for in Rietveld analysis.

III. RESULTS AND DISCUSSION

To obtain more detailed information about the evolution of the average crystal structure with temperature, the experimental XRD patterns were subjected to Rietveld analysis. The analysis was performed using the software GSAS II [51]. Exemplary results of Rietveld analysis of patterns obtained during cooling of the sample are shown in Fig. 2. Exemplary results of Rietveld analysis of patterns obtained during a subsequent warming of the sample are shown in Fig. 3. As can be seen in Fig. 2, diffraction patterns for as-synthesized MoTe₂ collected at temperature above 240 K are well fit by a model based on the monoclinic $1T'$ structure. The diffraction pattern obtained at 150 K, i.e., well below T_c , is relatively well fit by a model based on the orthorhombic T_d -type structure. The pattern obtained at 200 K upon cooling, however, exhibits weak signatures of splitting of the Bragg peaks at 2.4° and 2.65°, and hence, is difficult to be reproduced well by the T_d model alone. As can be seen in Fig. 3, the $1T'$ structure is not fully recovered until the sample is warmed to 350 K. Overall, results of Rietveld analysis indicate that some features of the monoclinic $1T'$ structure survive below T_c , where the average crystal structure appears to be of the orthorhombic T_d type. Also, the diffraction patterns of as-synthesized and

reconstructed $1T'$ -MoTe₂ phases appear significantly different at room temperature, indicating the presence of thermal hysteresis effects in the atomic rearrangement accompanying the reversible $1T'$ to T_d phase transition in MoTe₂.

To obtain more detailed information about the evolution of the local atomic structure with temperature, we conducted atomic pair distribution function (PDF) analysis [43,44]. In particular, we collected another set of diffraction patterns, this time positioning the 2D detector 300 mm away from the sample. This experimental arrangement allowed us to collect diffraction data to q values as high as 30 Å⁻¹, which is important for obtaining atomic PDFs with high real-space resolution (see Fig. S1 in Supplemental Material [52]). Atomic PDFs were derived from the patterns using well-established procedures [53], as explained in Supplemental Material [52]. The PDFs are summarized in Fig. 4. Selected atomic PDFs are shown over an extended range of r values in Figs. 5 and 6.

As can be seen in Figs. 4–6, the experimental atomic PDFs for studied MoTe₂ show well-defined peaks to high real-space distances. The observation indicates that it has a well-defined local atomic structure over a broad temperature range, including the $1T'$ to T_d phase transition. PDF peaks positioned at distances within the unit cell of $1T'$ and T_d phases, i.e., at distances <15 Å, exhibit fine changes with temperature [see

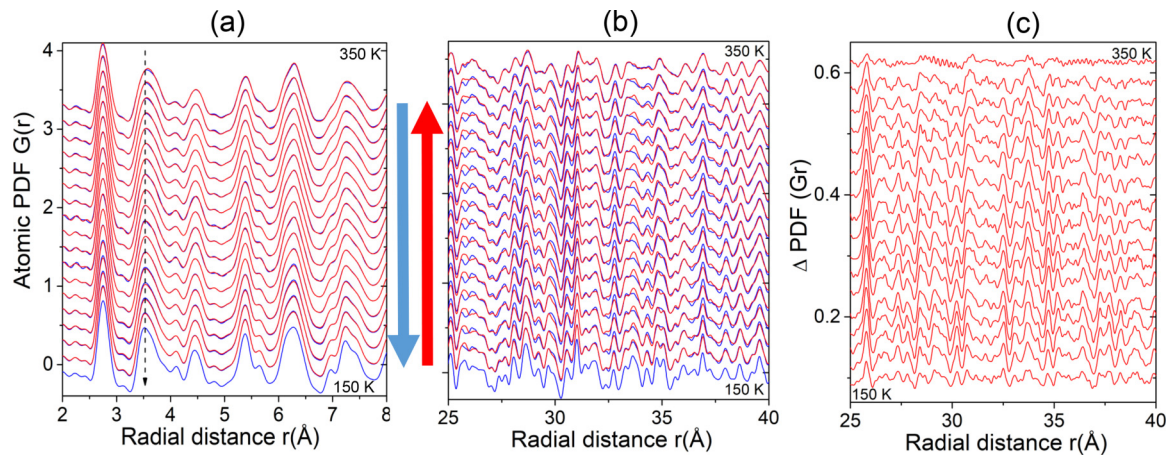


FIG. 4. (a) Low- r part of atomic PDFs for MoTe_2 phases obtained at different temperature during cooling (blue line) the sample from 350 to 150 K and then warming it (red line) back to 350 K. The temperature sequences are those shown in Figs. 1(c) and 1(d), respectively. The first PDF peak is positioned at about 2.9 Å. It reflects first-neighbor Mo-Mo and Mo-Te distances involving adjacent Mo-Te_6 octahedra. Also, it does not change much with temperature, indicating that, barring a small contraction/expansion, the octahedra do not change significantly during the reversible $1T'$ to T_d phase transition. The second PDF peak at about 3.5 Å reflects second-neighbor Mo-Mo and near-neighbor Te-Te distances. Its shape appears different at 150 and 350 K (follow the vertical black arrow) because interlayer Te-Te distances in $1T'$ and T_d phases are different, as shown in Fig. 1. (b) PDF peaks appearing at longer distances are sharp both above and below T_c , indicating that Te-Mo-Te layers do not undergo an unusual buckling [39] during the phase transition. The peaks, however, exhibit a clear thermal hysteresis effect. The effect is highlighted in (c), where the intensity difference, Δ PDF, between PDFs obtained at the same temperature once upon cooling and a second time upon warming the sample is given. The effect is seen practically all over the temperature interval accessed in the present studies.

Fig. 4(a)]. PDF peaks positioned at longer r distances change markedly with temperature, and also exhibit clear thermal hysteresis effects [see Figs. 4(b) and 4(c)]. To reveal what causes the changes, the atomic PDFs were fit with structure models based on the $1T'$ and T_d structures using the software PDFGUI [54]. Note that, as defined and obtained, PDFs reflect structural information from all physically meaningful components of the diffraction data used for their derivation. As a result, fits to experimental PDFs are sensitive to both the average crystal structure, producing sharp Bragg peaks, and local structural imperfections, producing diffuse scattering. This is advantageous when characterizing changes in the atomic arrangement in $1T'$ - MoTe_2 and T_d - MoTe_2 because the two phases are built of similar Te-Mo-Te layers that can slide with respect to each other leading to local variations in the layer stacking sequence, i.e., stacking faults. The approach is different from the traditional Rietveld analysis of diffraction data in reciprocal space, where diffuse scattering is largely neglected and, typically, phase analysis is based on a relatively small number of strong, low-angle Bragg peaks. Exemplary fits to PDFs obtained during cooling as-synthesized $1T'$ - MoTe_2 down to 150 and then warming it up to 350 K are shown in Figs. 5 and 6, respectively.

As can be seen in Fig. 5, and in line with the findings of Rietveld analysis shown in Fig. 2(a), the PDFs for as-synthesized $1T'$ - MoTe_2 obtained at 300 and 250 K, i.e., above T_c , can be very well reproduced by a structure model based on a monoclinic (S.G. $P2_1/m$) structure. Notably, the model reproduces the experimental data over a broad range of real-space distances, including atomic pair correlations within (<15 Å) and well beyond the crystallographic unit cell (15–60 Å). The monoclinic structure alone, however, does not reproduce well the experimental PDF data obtained below T_c . The

low- r part of these PDF data is well reproduced by an orthorhombic (S.G. $Pnm2_1$) structure model. The orthorhombic model, however, fails to reproduce well atomic pair correlations beyond the crystallographic unit cell at any temperature down to 150 K.

As can be seen in Fig. 6, upon warming, atomic pair correlations within the crystallographic unit cell remain orthorhombiclike below and appear monocliniclike above 240 K, respectively. However, up to 300 K, atomic correlations beyond the crystallographic unit cell cannot be described well either by the monoclinic or orthorhombic model alone. In line with results from Rietveld analysis, PDF fit results show that the monoclinic type of $1T'$ - MoTe_2 crystal structure is indeed completely recovered upon warming only after the temperature reaches 350 K (see Supplemental Material, Fig. S2 [52]).

Lattice parameters obtained by Rietveld analysis of XRD patterns are summarized in Fig. 7. An orthorhombic (S.G. $Pnm2_1$)-type model was used to fit the XRD patterns obtained below T_c and a monoclinic-type model (S.G. $P2_1/m$) model was used to fit the XRD patterns above T_c . The major difference between the models is the value of angle β , which is 90° for the former and approximately 93.8° for the latter. Also shown in Fig. 7 are lattice parameters derived by fits to low- r PDF data (<15 Å), which are very sensitive to atomic correlations within the crystallographic unit cell of $1T'$ - MoTe_2 and T_d - MoTe_2 . The goodness of fit indicators, R_w [52], for the PDF fits are summarized in Figs. 8(a) and 8(b). Data for R_w show that the crystallographic unit cell of studied MoTe_2 phases is indeed predominantly orthorhombic and monoclinic below and above T_c , respectively. Rietveld and PDF fit-derived lattice parameters shown in Fig. 7 are seen to exhibit a discontinuity at $T_c = 240$ K, indicating that,

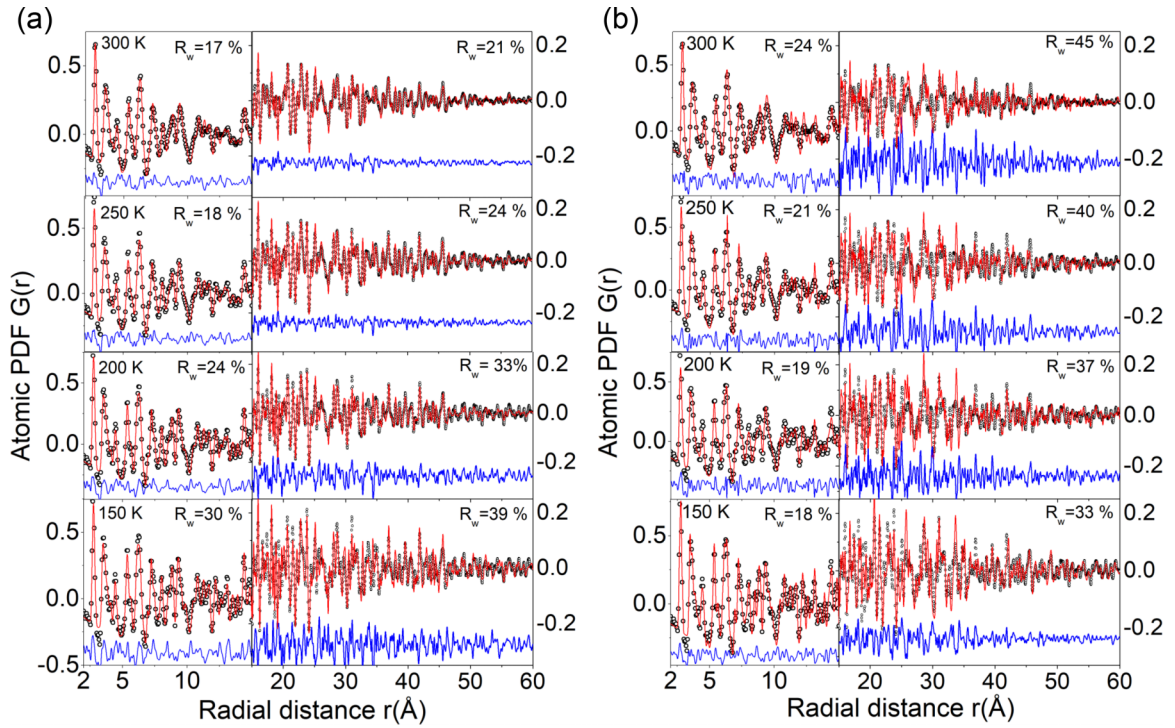


FIG. 5. Structure model fits (red line) to experimental atomic PDFs (symbols) obtained at different temperature during cooling the sample from 350 to 150 K. The residual difference (blue line) is shifted by adding a negative constant for clarity. Fits in (a) are based on a monoclinic ($1T'$ -type) structure model. Fits in (b) are based on an orthorhombic (T_d -type) structure model. The fits are performed over a range of r values from 2 to 60 Å. For each dataset, results of the fit to low- (2 to 15 Å) and higher- r (15 to 60 Å) PDF parts are shown side by side on a different scale. Goodness of fit factors R_w are also shown. Note that the c -axis lattice parameter for both $1T'$ and T_d phases is about 14 Å. Thus, fits to the low- r PDF part are particularly sensitive to atomic pair correlations within the crystallographic unit cell of the phases. Fits results indicate that the crystallographic unit cell is of a monoclinic (S.G. $P2_1/m$) type ($R_w < 20\%$) above T_c ($= 240$ K). It increasingly becomes orthorhombic (S.G. $Pnm2_1$) like ($R_w < 20\%$) when the temperature is decreased below T_c . Furthermore, above T_c , atomic correlations both within and beyond the crystallographic unit cell are of the same monoclinic type (the respective R_w values are both low and comparable in magnitude). Below T_c , however, atomic correlations beyond the crystallographic unit cell are not entirely either monoclinic or orthorhombic in character, because both the respective R_w values ($> 30\%$) and the residual difference are large. Note that the quality of fit, as estimated in terms of R_w factors, for the low- r part of atomic PDFs obtained at 300 and 150 K is comparable to that achieved in Ref. [46].

macroscopically, the phase transition between the $1T'$ and T_d phases is first order both upon cooling and warming.

Results from fits to higher- r PDF data (15 – 60 Å), however, show that the interatomic correlations beyond the crystallographic unit cell are not well reproduced either by the monoclinic or orthorhombic model alone below 240 K upon cooling and up to 300 K upon warming. Therefore, we approached the higher- r part of atomic PDFs obtained in this temperature range by a model featuring a mixture of $1T'$ and T_d phases, which, locally, appears as a mixture of coexisting monoclinic ($1T'$ type) and orthorhombic (T_d type) stacking sequences of near-identical Te-Mo-Te layers. The model performed very well as the exemplary PDF fits in Fig. 9 show. The relative percentage of monoclinic-type stacking sequence [Fig. 1(b) in the studied MoTe_2 phases is shown in Fig. 8(c). As can be seen in the figure, a large portion of Te-Mo-Te layers in the orthorhombic T_d phase appear stacked in a sequence characteristic to the monoclinic $1T'$ phase down to 150 K, i.e., down to almost 100 K below T_c . Also, contrary to the case of as-synthesized $1T'$ - MoTe_2 phase, a significant portion of Te-Mo-Te layers in the reconstructed $1T'$ phase appear stacked in a sequence characteristic of the orthorhombic T_d

phase up to 350 K, i.e., up to about 100 K above T_c . Lastly, the relative ratio of the monoclinic to orthorhombic stacking sequence in the studied phases is seen to evolve continuously across T_c and also exhibit a broad thermal hysteresislike effect [see Fig. 8(c)].

IV. CONCLUSION

The picture emerging from the results of our study is as follows: Though metastable at room temperature, as-synthesized $1T'$ - MoTe_2 may appear largely free from structural imperfections at atomic level. Upon cooling down, continuously, layers in $1T'$ - MoTe_2 slide with respect to each other, forming an orthorhombic-type stacking sequence. The average crystal symmetry, as revealed by Rietveld analysis of XRD data, and the crystallographic unit cell, as revealed by analysis of low- r atomic PDF data, become predominantly orthorhombic at $T_c = 240$ K. Upon further cooling, the relative percentage of monoclinic-type stacking of Te-Mo-Te layers in the emerged T_d phase keeps diminishing but remains very substantial down to 150 K, as revealed by analysis of the higher- r part of atomic PDFs. Upon a subsequent warming, the relative percentage of

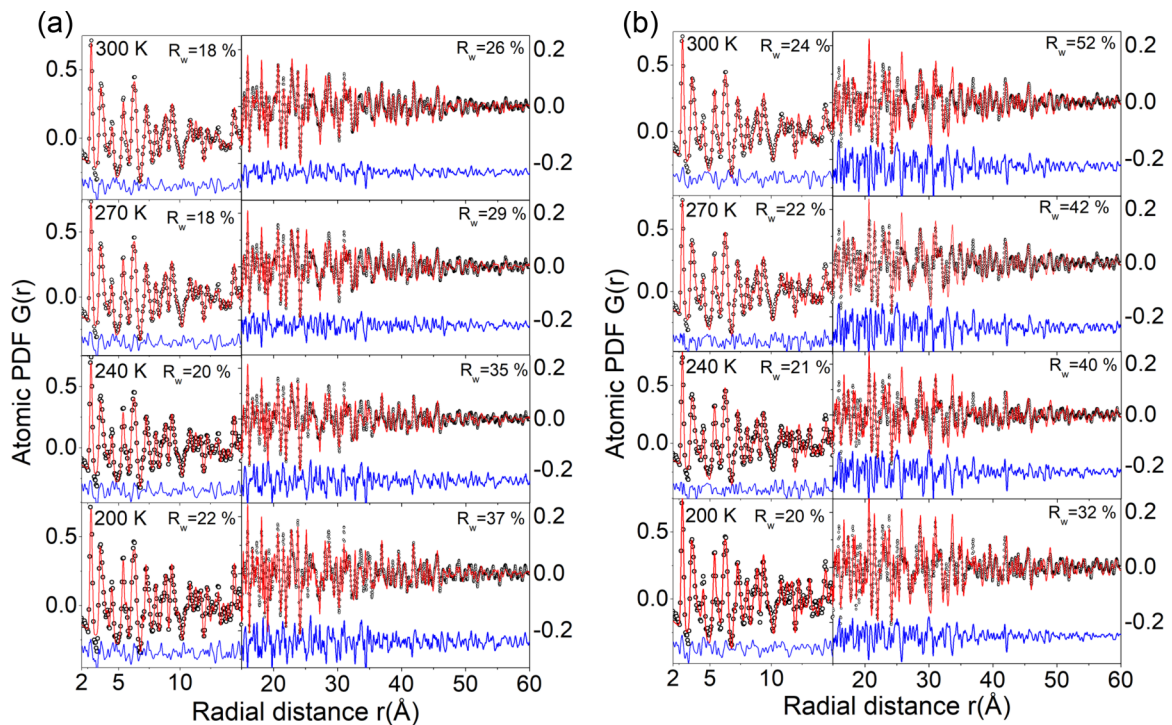


FIG. 6. Structure model fits (red line) to experimental atomic PDFs (symbols) obtained at different temperature during warming the sample from 150 to 350 K. The residual difference (blue line) is shifted by adding a negative constant for clarity. Fits in (a) are based on a monoclinic ($1T'$ -type) structure model. Fits in (b) are based on an orthorhombic (T_d -type) model structure. The fits are performed over an r range from 2 to 60 Å. For each dataset, results of the fit to low- (2 to 15 Å) and higher- r (15 to 60 Å) PDF parts are shown side by side on a different scale. Goodness of fit factors R_w are also shown. Note that the c -axis lattice parameter for both $1T'$ and T_d phases is about 14 Å. Thus, fits to low- r PDF part are particularly sensitive to atomic pair correlations within the unit cell of the phases. Fits results indicate that the crystallographic unit cell at 200 K is of an orthorhombic (S.G. $Pnm2_1$) type ($R_w = 20\%$ for the orthorhombic vs 22% for the monoclinic) and increasingly becomes monocliniclike (S.G. $P2_1/m$ -type) with increasing temperature ($R_w = 18\%$ for the monoclinic vs 24% for the orthorhombic model at 300 K). At any temperature, neither the monoclinic nor the orthorhombic model alone can reproduce well the atomic correlations beyond the crystallographic unit cell (the respective R_w values are above 30% and the residual difference is large).

layers stacked monoclinically increases steadily but reaches 100% only when the temperature is increased to about 350 K, that is, a considerable fraction of layers in the reconstructed $1T'$ phase remain stacked orthorhombically up to about 100 K above T_c . Here it may be mentioned that recent neutron-scattering studies on MoTe_2 monocrystals indicated that, upon warming, monoclinically- and orthorhombicallylike stacked Te-Mo-Te layers may form a pseudo-orthorhombic polar superstructure near T_c [50]. A structure model based on that superstructure does not perform much better than either the monoclinic or orthorhombic models does alone and definitely is not as good in reproducing the experimental PDF data as the “intermixed stacking sequences” model considered here (see Supplementary Fig. 3 in Ref. [52]). However, our results do not completely rule out the possibility of a spontaneous formation of superstructures of monoclinically- and orthorhombicallylike stacked Te-Mo-Te layers near the reversible $1T'$ to T_d phase transition. Likely, such a formation would strongly depend on the thermal prehistory of the studied sample. More studies are required in this regard.

The main difference between the $1T'$ and T_d phases of MoTe_2 is the stacking of Te-Mo-Te planes, which is largely controlled by van der Waals interactions. Though weak in general, the interactions appear to sustain coexisting $1T'$ -

and T_d -type stacking over a broad temperature range. The coexistence would cause the electronic and lattice excitations in the T_d and recovered $1T'$ phases to exist in locally mixed states with respect to lattice polarity, likely making trivial and topological electronic phenomena intrinsically entangled. It has to be recognized that even though the reversible $1T'$ to T_d phase transition appears first order macroscopically, as indicated by the disappearance of splitting of Bragg diffraction peaks and presence of discontinuity in the lattice parameters, it is continuous locally, i.e., second-order like, as indicated by the gradual evolution of the relative percentage of $1T'$ - vs T_d -type stacking of Te-Mo-Te layers near T_c . This smears changes in the electronic and thermal transport properties accompanying the transition by introducing a landscape of transition temperatures. Under such conditions, the kinetics of the $1T'$ to T_d phase transition can be hindered and hence the system adopt a metastable state persisting far below the transition temperature, which is different from a macroscopic phase segregation. Because this state may vary from sample to sample, experimental data and theoretical predictions envisioning a perfect crystal structure may be difficult to reconcile. Furthermore, the presence of coexisting local polar and non-polar regions in this state, including the resulting variety of internal interfaces where the spatial symmetry is broken, may

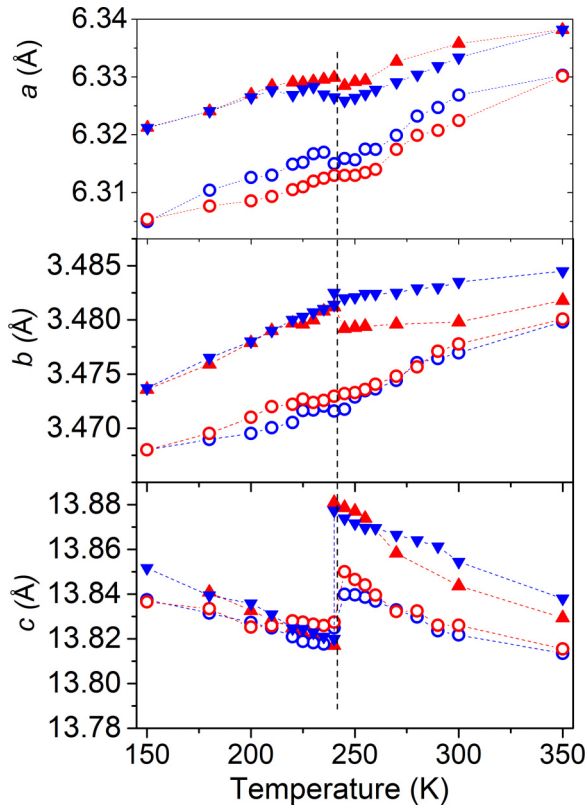


FIG. 7. Evolution of lattice parameters for MoTe_2 phases during cooling (blue symbols) the sample from 350 down to 150 K followed by warming it (red symbols) back to 350 K. Data are derived through Rietveld fits to high-energy XRD data (circles) (e.g., see Figs. 2 and 3) and fits to the low- r part (2 to 15 Å) of atomic PDFs (triangles) (e.g. see Fig. 5 and 6) obtained at the respective temperature. The crystallographic unit cell above 240 K is monoclinic with lattice parameters $a \neq b \neq c$, and monoclinic angles $\alpha = \gamma = 90^\circ$ and $\beta \approx 93.8^\circ$. The crystallographic unit cell below 240 K is orthorhombic with lattice parameters $a \neq b \neq c$ and angles $\alpha = \beta = \gamma = 90^\circ$. Barring small differences in the position of atoms, the major difference between the two unit cells is that the former is inclined and the latter is not [see Figs. 1(a) and 1(b)]. The experimental lattice parameters show a clear hysteresis and a more (c parameter) or less (a and b parameters) pronounced discontinuous change at 240 K, indicating that the $1T'$ to T_d phase transition is first order. Also, the lattice parameters derived through Rietveld analysis appear somewhat shorter than those derived through fits to atomic PDFs. Difference between Rietveld and PDF analysis-derived lattice parameters may appear because the former does not and the latter accounts for the diffuse component of the diffraction data [44,45]. Note that, for clarity, the unit-cell parameters for the T_d phase are reported not in the standard $(\vec{a}, \vec{b}, \vec{c})$ S.G. $Pnm2_1$ setting but in the symmetry-equivalent $(\vec{b}, \vec{a}, \vec{c})$ S.G. $Pnm2_1$ setting.

indeed be behind some of the unusual properties of T_d - MoTe_2 . Recent high-pressure neutron-diffraction studies on the $1T'$ to T_d phase transition came to a similar conclusion and described the possible metastable state as a network of inner $1T'/T_d$ interfaces [57]. Therefore, achieving control over not only the average but also local crystal structure of T_d - MoTe_2 , particularly in terms of relative percentage and pattern of stacking faults, would allow us to explore novel physics, including new

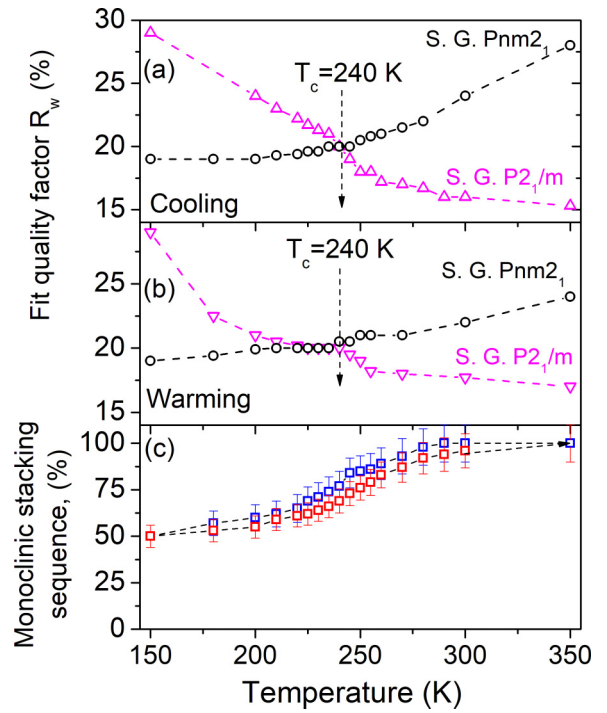


FIG. 8. Goodness of fit indicators, R_w , for fits to the low- r part of atomic PDFs (2-15 Å) obtained during (a) cooling and then (b) warming the sample. The fits are based on a monoclinic (S.G. $P2_1/m$; magenta triangles) and orthorhombic (S.G. $Pnm2_1$; black circles) unit cells. The results clearly show that the crystallographic unit cell is essentially orthorhombic below and monoclinic above 240 K. The black and magenta broken lines are a guide to the eye. (c) Change in the relative percentage of local monoclinic vs orthorhombiclike stacking of Te-Mo-Te layers during cooling (blue symbols) and warming (red symbols) the sample. The percentage exhibits a broad thermal hysteresislike effect and changes continuously across the transition temperature, consistent with a second-order transition behavior. Notably, signatures of local orthorhombiclike stacking appear in $1T'$ - MoTe_2 above T_c upon cooling and persist well above T_c upon warming. Also, the percentage of monocliniclike stacking in the T_d phase remains rather high at 150 K, i.e., 100 K below T_c . For reference, macroscopically, the T_d phase appears orthorhombic at 150 K, as indicated by the lack of splitting in the $(112)_O$ Bragg peak [Fig. 1(e)] and good quality of Rietveld analysis of the respective XRD pattern in terms of an orthorhombic structure [see Fig. 2(b)]. When the trend of data in (c) is extrapolated smoothly toward low temperature, that percentage appears to approach zero well below 50 K. The vertical black arrow in (a) and (b) is a guide to the eye.

geometries of the Fermi surface and Weyl semimetal states in proximity of superconductivity, warranting further investigations. The investigations will benefit from nontraditional techniques for atomic structure characterization as the atomic PDF analysis employed here.

ACKNOWLEDGMENTS

This work was supported by the U.S. Department of Energy, Office of Science, Office of Basic Energy Sciences under Award No. DE-SC0006877 and used resources of

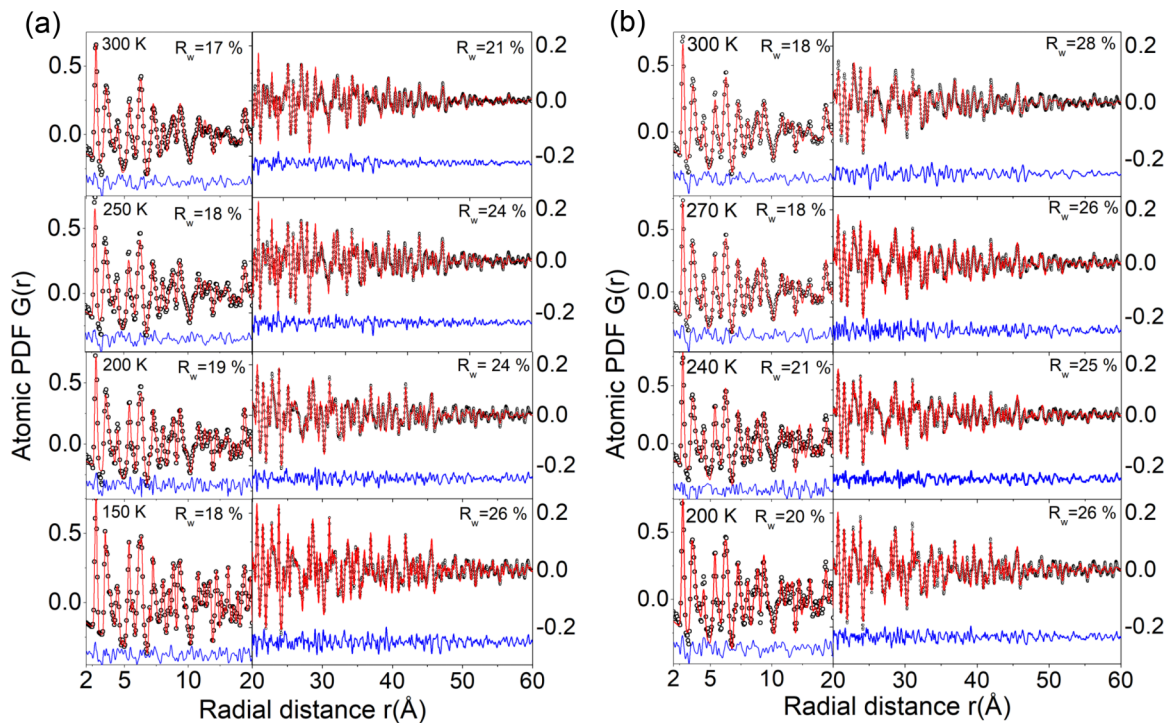


FIG. 9. Structure model fits (red line) to experimental atomic PDFs (symbols) obtained during (a) cooling and (b) warming the sample. The residual difference (blue line) is shifted by adding a negative constant for clarity. For each dataset, results of the fit to low- (2 to 15 Å) and higher- r (15 to 60 Å) PDF parts are shown side by side on a different scale. Goodness of fit factors R_w are also shown. The model features a mixture of locally coexisting monoclinic ($1T'$ -type) and orthorhombic (T_d -type) stacking sequences of Te-Mo-Te layers. The relative percentage of the two sequences is shown in Fig. 8(c). The quality of the fits at higher- r values is outstanding comparing to the single-phase model fits in Figs. 5 and 6.

the Advanced Photon Source, a U.S. Department of Energy (DOE) Office of Science User Facility operated for the DOE Office of Science by Argonne National Laboratory

under Contract No. DE-AC02-06CH11357. Thanks are due to K. Chapagain for the help with Rietveld analysis of XRD data.

- [1] F. C. Chen, H. Y. Lv, X. Luo, W. J. Lu, Q. L. Pei, G. T. Lin, Y. Y. Han, X. B. Zhu, W. H. Song, and Y. P. Sun, *Phys. Rev. B* **94**, 235154 (2016).
- [2] Q. L. Pei, W. J. Meng, X. Luo, H. Y. Lv, F. C. Chen, W. J. Lu, Y. Y. Han, P. Tong, W. H. Song, Y. B. Hou, Q. Y. Lu, and Y. P. Sun, *Phys. Rev. B* **96**, 075132 (2017).
- [3] S. Thirupathiah, R. Jha, B. Pal, J. S. Matias, P. K. Das, P. K. Sivakumar, I. Vobornik, N. C. Plumb, M. Shi, R. A. Ribeiro, and D. D. Sarma, *Phys. Rev. B* **95**, 241105(R) (2017).
- [4] S. Lee, J. Jang, S.-I. Kim, S.-G. Jung, J. Kim, S. Cho, S. W. Kim, J. Y. Rhee, K.-S. Park, and T. Park, *Sci. Rep.* **8**, 13937 (2018).
- [5] F. C. Chen, X. Luo, J. Yan, Y. Sun, H. Y. Lv, W. J. Lu, C. Y. Xi, P. Tong, Z. G. Sheng, X. B. Zhu, W. H. Song, and Y. P. Sun, *Phys. Rev. B* **98**, 041114(R) (2018).
- [6] Y. Zhang, J. van den Brink, C. Felser, and B. Yan, *2D Mater.* **5**, 044001 (2018).
- [7] X. Qian, J. Liu, L. Fu, and J. Li, *Science* **346**, 1344 (2014).
- [8] S. Lim, C. R. Rajamathi, V. Süß, C. Felser, and A. Kapitulnik, *Phys. Rev. B* **98**, 121301(R) (2018).
- [9] Y. Zhang, Y. Sun, and B. Yan, *Phys. Rev. B* **97**, 041101(R) (2018).
- [10] J. Zhou, J. Qiao, A. Bournel, and W. Zhao, *Phys. Rev. B* **99**, 060408(R) (2019).
- [11] C. Heikes, I.-L. Liu, T. Metz, C. Eckberg, P. Neves, Y. Wu, L. Hung, P. Piccoli, H. Cao, J. Leao, J. Paglione, T. Yildirim, N. P. Butch, and W. Ratcliff, *Phys. Rev. Mater.* **2**, 074202 (2018).
- [12] S. Yuan, X. Luo, H. L. Chan, C. Xiao, Y. Dai, M. Xie, and J. Hao, *Nat. Commun.* **10**, 1775 (2019).
- [13] F.-T. Huang, S. J. Lim, S. Singh, J. Kim, L. Zhang, J.-W. Kim, M.-W. Chu, K. M. Rabe, D. Vanderbilt, and S.-W. Cheong, *Nat. Commun.* **10**, 4211 (2019).
- [14] H. Takahashi, T. Akiba, K. Imura, T. Shiino, K. Deguchi, N. K. Sato, H. Sakai, M. S. Bahramy, and S. Ishiwata, *Phys. Rev. B* **95**, 100501(R) (2017).
- [15] Y. Qi, P. G. Naumov, M. N. Ali, C. R. Rajamathi, W. Schnelle, O. Barkalov, M. Hanfland, S.-Ch. Wu, C. Shekhar, Y. Sun, V. Su, M. Schmidt, U. Schwarz, E. Pippel, P. Werner, R. Hillebrand, T. Forster, E. Kampert, S. Parkin, R. J. Cava, C. Felser, B. Yan, and S. A. Medvedev, *Nat. Commun.* **7**, 11038 (2016).
- [16] Y. Sun, S.-C. Wu, M. N. Ali, C. Felser, and B. Yan, *Phys. Rev. B* **92**, 161107(R) (2015).

- [17] A. A. Soluyanov, D. Gresch, Z. Wang, Q. Wu, M. Troyer, X. Dai, and B. A. Bernevig, *Nature (London)* **527**, 495 (2015).
- [18] L. Huang, T. M. McCormick, M. Ochi, Z. Zhao, M.-T. Suzuki, R. Arita, D. M. Y. Wu, H. Cao, J. Yan, N. Trivedi, and A. Kaminski, *Nat. Mater.* **15**, 1155 (2016).
- [19] Z. Wang, D. Gresch, A. A. Soluyanov, W. Xie, S. Kushwaha, X. Dai, M. Troyer, R. J. Cava, and B. A. Bernevig, *Phys. Rev. Lett.* **117**, 056805 (2016).
- [20] K. Deng, G. Wan, P. Deng, K. Zhang, S. Ding, E. Wang, M. Yan, H. Huang, H. Zhang, Z. Xu, J. Denlinger, A. Fedorov, H. Yang, W. Duan, H. Yao, Y. Wu, S. Fan, H. Zhang, X. Chen, and S. Zhou, *Nat. Phys.* **12**, 1105 (2016).
- [21] A. Tamai, Q. S. Wu, I. Cucchi, F. Y. Bruno, S. Riccò, T. K. Kim, M. Hoesch, C. Barreteau, E. Giannini, C. Besnard, A. A. Soluyanov, and F. Baumberger, *Phys. Rev. X* **6**, 031021 (2016).
- [22] D. Rhodes, R. Schönemann, N. Aryal, Q. Zhou, Q. R. Zhang, E. Kampert, Y.-C. Chiu, Y. Lai, Y. Shimura, G. T. McCandless, J. Y. Chan, D. W. Paley, J. Lee, A. D. Finke, J. P. C. Ruff, S. Das, E. Manousakis, and L. Balicas, *Phys. Rev. B* **96**, 165134 (2017).
- [23] A. Crepaldi, G. Autes, G. Gatti, S. Roth, A. Sterzi, G. Manzoni, M. Zacchigna, C. Cacho, R. T. Chapman, E. Springate *et al.*, *Phys. Rev. B* **96**, 241408(R) (2017).
- [24] S. Singh, J. Kim, K. M. Rabe, and D. Vanderbilt, *Phys. Rev. Lett.* **125**, 046402 (2020).
- [25] H.-J. Kim, S.-H. Kang, I. Hamada, and Y.-W. Son, *Phys. Rev. B* **95**, 180101(R) (2017).
- [26] A. V. Kolobov and J. Tominaga, *Two-Dimensional Transition-Metal Dichalcogenides*, Vol. 239 (Springer, Berlin, 2016).
- [27] J. Jiang, Z. K. Liu, Y. Sun, H. F. Yang, C. R. Rajamathi, Y. P. Qi, L. X. Yang, C. Chen, H. Peng, C.-C. Hwang, S. Z. Sun, S.-K. Mo, I. Vobornik, J. Fujii, S. S. P. Parkin, C. Felser, B. H. Yan, and Y. L. Chen, *Nat. Commun.* **8**, 13973 (2017).
- [28] K. F. Mak, C. Lee, J. Hone, J. Shan, and T. F. Heinz, *Phys. Rev. Lett.* **105**, 136805 (2010).
- [29] Q. H. Wang, K. Kalantar-Zadeh, A. Kis, J. N. Coleman, and M. S. Strano, *Nat. Nanotechnol.* **7**, 699 (2012).
- [30] L. F. Mattheiss, *Phys. Rev. B* **8**, 3719 (1973).
- [31] R. Clarke, E. Marseglia, and H. P. Hugues, *Philos. Mag.* **38**, 121 (1978).
- [32] D. H. Keum, S. Cho, J. H. Kim, D.-H. Choe, H.-J. Sung, M. Kan, H. Kang, J.-Y. Hwang, S. W. Kim, H. Yang, K. J. Chang, and Y. H. Lee, *Nat. Phys.* **11**, 482 (2015).
- [33] G. Eda, T. Fujita, H. Yamaguchi, D. Voiry, M. Chen, and M. Chhowalla, *ACS Nano* **6**, 7311 (2012).
- [34] C.-X. Liu, S.-C. Zhang, and X.-L. Qi, *Ann. Rev. Condens. Matter Phys.* **7**, 301 (2016).
- [35] L. X. Yang, Z. K. Liu, Y. Sun, H. Peng, H. F. Yang, T. Zhang, B. Zhou, Y. Zhang, Y. F. Guo, M. Rahn, D. Prabhakaran, Z. Hussain, S.-K. Mo, C. Felser, B. Yan, and Y. L. Chen, *Nat. Phys.* **11**, 728 (2015).
- [36] X.-J. Yan, Y.-Y. Lv, L. Li, X. Li, Sh.-H. Yao, Y.-B. Chen, L. X.-P. H. Lu, M.-H. Lu, and Y.-F. Chen, *npj Quant. Mater.* **2**, 31 (2017).
- [37] J. A. Schneeloch, C. Duan, J. Yang, J. Liu, X. Wang, and D. Louca, *Phys. Rev. B* **99**, 161105(R) (2019).
- [38] C. Manolikas, J. van Landuyt, and S. Amelinckx, *Phys. Status Solidi* **53**, 327 (1979).
- [39] V. Petkov, J. Yang, S. Shastri, and Y. Ren, *Phys. Rev. B* **102**, 134119 (2020).
- [40] F. Hulliger in *Structural Chemistry of Layer-type Phases*, edited by F. Levy (D. Riedel, Dordrecht, 1976).
- [41] A. Zhang, X. Ma, C. Liu, R. Lou, Y. Wang, Q. Yu, Y. Wang, T.-L. Xia, S. Wang, L. Zhang, X. Wang, Ch. Chen, and Q. Zhang, *Phys. Rev. B* **100**, 201107(R) (2019).
- [42] A. P. Weber, P. Russmann, N. Xu, S. Muff, M. Fanciulli, A. Magrez, P. Bugnon, H. Berger, N. C. Plumb, M. Shi, S. Blügel, P. Mavropoulos, and J. H. Dil, *Phys. Rev. Lett.* **121**, 156401 (2018).
- [43] T. Egami and S. J. L. Billinge, *Underneath the Bragg Peaks: Structural Analysis of Complex Materials* (Pergamon, Oxford, UK, 2003).
- [44] V. Petkov, in *Characterization of Materials* (John Wiley & Sons, New York, 2003).
- [45] V. Petkov, K. Chapagain, S. Shastri, and Y. Ren, *Phys. Rev. B* **101**, 121114(R) (2020).
- [46] Z. Guguchia, F. von Rohr, Z. Shermadini, A. T. Lee, S. Banerjee, A. R. Wieteska, C. A. Marianetti, B. A. Frandsen, H. Luetkens, Z. Gong, S. C. Cheung, C. Baines, A. Shengelaya, G. Taniashvili, A. N. Pasupathy, E. Morenzoni, S. J. L. Billinge, A. Amato, R. J. Cava, R. Khasanov, and Y. J. Uemura, *Nat. Commun.* **8**, 1082 (2017).
- [47] See <https://www.2dsemiconductors.com/metallic-mote2/#description>.
- [48] N. G. Wright, R. J. Nelves, S. A. Belmonte, and M. I. McMahon, *J. Synchrotron Rad.* **3**, 112 (1996).
- [49] S. Vishwanath, A. Sundar, X. Liu, A. Azcatl, E. Lochocki, A. R. Woll, S. Rouvimov, W. S. Hwang, N. Lu, X. Peng, H.-H. Lien, J. Weisenberger, S. McDonnell, M. J. Kim, M. Dobrowolska, J. K. Furdyna, K. Shen, R. M. Wallace, D. Jena, and H. G. Xing, *J. Cryst. Growth* **482**, 61 (2018).
- [50] Y. Tao, J. A. Schneeloch, Ch. Duan, M. Matsuda, S. E. Dissanayake, A. A. Aczel, J. A. Fernandes-Baca, F. Ye, and D. Louca, *Phys. Rev. B* **100**, 100101(R) (2019).
- [51] B. H. Toby and R. B. & Von Dreele, *J. Appl. Crystallogr.* **46**, 544 (2013).
- [52] See Supplemental Material at <http://link.aps.org/supplemental/10.1103/PhysRevB.103.094101> for experimental x-ray diffraction patterns, atomic pair distribution functions and refined lattice parameters.
- [53] V. Petkov, *J. Appl. Crystallogr.* **22**, (1989) 387.
- [54] C. L. Farrow, P. Juhás, J. W. Liu, D. Bryndin, E. S. Božin, J. Bloch, T. Proffen, and S. J. L. Billinge, *J. Phys.: Condens. Matter* **19**, 335219 (2007).
- [55] A. M. Vora, *J. Semicond.* **33**, 062001 (2012).
- [56] R. Pratap, *J. Mater. Sci.* **9**, 1011 (1974).
- [57] I.-L. Liu, C. Heikes, T. Yildirim, C. Eckberg, T. Mrtz, H. Kim, Sh. Ran, W. D. Ratcliff, J. Paglione, and N. P. Butch, *npj Quant. Mater.* **5**, 62 (2020).